JOURNAL OF Materials CHEMISTRY

Microstructure of $Li_{1+x}Mn_{2-x}O_4$ spinels obtained from metal–organic precursors

Ekaterina N. Zhecheva,* Mila Y. Gorova and Radostina K. Stoyanova

Institute of General and Inorganic Chemistry, Bulgarian Academy of Sciences, 1113 Sofia, Bulgaria. E-mail: banchem@bas.bg

Received 4th January 1999, Accepted 12th April 1999

A metal–organic precursor method was adopted for the preparation of lithium–manganese spinel oxides. EPR spectra of Mn^{2+} in solutions and in freeze-dried compositions, as well as IR and DSC of freeze-dried compositions, show that α-hydroxyorganic acids (such as lactic, malic and citric acids) chelate Mn^{2+} *via* hydroxy and carboxylate groups. At 450 °C, thermal decomposition of Li–Mn–organic acid precursors with Li/Mn = 1.05/1.95 leads to the formation of non-stoichiometric $Li[Li_yMn_{2-y-\delta}\square_\delta]O_4$ spinels ($0.03 < y < 0.05$; $0.02 < \delta < 0.05$). EPR of Mn^{4+} was used to throw light on the microstructure of the spinels obtained. For the annealed spinels at 750 °C there is a transition from uniform to non-uniform distribution of the excess Mn^{4+} ions and the corresponding metal vacancies. As a result, the bulk of the spinel becomes close to the stoichiometric composition $Li[Li_{0.05}Mn_{1.95}]O_4$, whereas the spinel surface accommodates the excess Mn^{4+} ions. The formation of Mn^{4+}-rich surface regions depends both on the cooling rate and on the organic acid used in the precursors. Lactate precursors are most appropriate for the preparation of lithium–manganese spinels with a homogeneous cation distribution.

1 Introduction

During the last decade investigations on the intercalation properties of the lithium–manganese spinels $Li_{1+x}Mn_{2-x}O_4$ were closely associated with the development of secondary lithium batteries.[1–3] From an economic and ecological point of view, $Li_{1+x}Mn_{2-x}O_4$ with $0.02 \leqslant x \leqslant 0.05$ are considered as the most promising cathode materials.[4,5] However, the drastic dependence of the electrochemical properties of $Li_{1+x}Mn_{2-x}O_4$ on the conditions of their synthesis restricts the large-scale production of lithium-ion batteries.[6,7]

Extensive studies have been devoted to the nonstoichiometry of $Li_{1+x}Mn_{2-x}O_4$,[5,8–14] but little work has been done to elucidate their microstructure.[15,16] $Li_{1+x}Mn_{2-x}O_4$ is able to accommodate a broad range of nonstoichiometry in the Li/Mn ratio, as well as in the oxygen content.[9–12] The stoichiometric $LiMn_2O_4$ is a normal spinel where Li and Mn occupy the tetrahedral and octahedral spinel sites, respectively.[8] With an increase of Li/Mn ratio, the tetrahedral sites remain unchanged, while the excess of lithium and the manganese reside in octahedral sites: $(T_d\text{-Li})[O_h\text{-Li}_x\text{Mn}_{2-x}]O_4$.[9–11] At the same time, it is possible to keep the Li/Mn ratio at the expense of the appearance of vacancies in tetrahedral and octahedral sites: $(T_d\text{-Li}_{1-\delta}\square_\delta)[O_h\text{-Mn}_{2-2\delta}\square_{2\delta}]O_4$.[12] The lithium–manganese spinels are prepared in two ways: by solid-phase and soft-chemistry reactions. The initial salts used in solid phase reactions are usually Li_2CO_3 and MnO_2, while soft-chemistry reactions involve mainly thermal decomposition of metal–organic precursors[17–27] or ion-exchange reactions.[28–30] For example, acetic,[17,18] oxalic,[19] succinic,[19] malonic,[19] tartaric,[20] citric,[21–23] acetylacetonate–propionic[24] and glycolic[25–27] acids are suitable precursors for the preparation of lithium–manganese spinels at low-temperatures (400 °C). With both synthesis approaches the initial thermal treatment and the rates of heating and cooling essentially affect the electrochemical properties of the spinels, the composition and the structure showing only a weak change. This observation can be correlated with the redox properties of Mn^{3+}/Mn^{4+} couples in spinels.

The drastic dependence of the electrochemical properties of the spinels on their synthesis conditions can be related to the spinel microstructure. In this respect, there is a need for an experimental method to monitor the spinel microstructure. The basic method used is X-ray analysis.[7,31,32] In addition, TGA analysis has been proposed for determining the exact Li/Mn ratio in the spinel composition.[33–35] Recently, EPR spectroscopy of Mn^{4+} has been shown as a powerful tool for studying the Mn^{4+} distribution in the octahedral spinel sublattice of $Li_{1+x}Mn_{2-x}O_4$.[36–38]

The purpose of the present work was to investigate the effect of metal–organic precursors on the composition and microstructure of lithium–manganese spinels. Taking into account the electrochemical properties of the spinels, we studied the spinel with a Li/Mn ratio of 1.05/1.95. This spinel was prepared *via* a metal–α-hydroxycarboxylate route, where the complex formation between Mn and the organic acids through polyfunctional groups allows the preparation and modification of the precursors at a molecular level. We have chosen the following α-hydroxycarboxylic acids: lactic acid [$CH_3CH(OH)CO_2H$ (lac)], malic acid [$HO_2CCH_2CH(OH)CO_2H$ (mal)] and citric acid [$HO_2CCH_2C(OH)(CO_2H)CH_2CO_2H$ (cit)]. The EPR studies of Mn^{4+} show the dependence of the microstructure of the spinel compositions on the synthesis conditions.

2 Experimental

2.1 Preparation of lithium–manganese α-hydroxycarboxylate precursors

Lithium–manganese complexes with lactic, malic and citric acid were obtained by dissolution of Li_2CO_3 and $MnCO_3$ in aqueous solutions of the corresponding organic acid (0.05 M). The Li : Mn : organic acid ratio was as follows: Li : Mn : lac = 1.05 : 1.95 : 6, Li : Mn : mal = 1.05 : 1.95 : 3, Li : Mn : cit = 1.05 : 1.95 : 2 and Li : Mn : cit = 1.05 : 1.95 : 4. Heating at 60 °C in an argon atmosphere led to the formation of clear solutions, which were concentrated to 0.1 M Mn. Under these conditions, stable solutions with pH = 4.5–5 were obtained for the first three compositions, whereas ammonia was added to the fourth composition up to pH values of 6.5–7. After complexation, the solutions were cooled to room temperature, then frozen instantly with liquid nitrogen and dried in vacuum (20–30 mbar) at −20 °C with an Alpha-Crist freeze-dryer. The solid phase obtained was heated in air at 450 °C for 5 h with a heating rate of 1 and of 10 °C min^{-1}. The samples were additionally annealed at 750 °C for 20 h in air, two regimes

being used for cooling to room temperature: (i) slow cooling at 1 °C min and (ii) quenching by pouring out the powder between two metal plates. In some cases after annealing at 750 °C, the samples were slow cooled to lower temperature (600 and 500 °C) and then quenched to room temperature. For the sake of convenience, the samples annealed at 750 °C will be denoted as slow cooled, quenched, or quenched from intermediate temperature samples. 'Standard' $Li_{1.05}Mn_{1.95}O_4$ and $LiMn_2O_4$ were obtained by a solid state reaction between γ-MnO_2 (Faradizer M) and Li_2CO_3 at 750 °C for 48 h, the samples being slow cooled and quenched. The chemical and structural data for standard samples match the data reported in literature.[7,9,13,39]

2.2 Sample characterisation

The lithium content in the samples was determined by atomic absorption analysis. The total manganese content was established complexometrically and by atomic absorption analysis. The organic complex compositions were analysed according to the standard procedure for C and H (as CO_2 and H_2O) and by the method of Dumas for N_2. The mean oxidation state of manganese ions was established by permanganometric titration.

The X-ray phase analysis was made by a Philips diffractometer with Cu-Kα radiation. The IR spectra were registered with a Specord-75 (ex-GDR) spectrometer in KBr tablets or in a suspension with Nujol. The specific surface area of the samples was determined by the BET method using low-temperature nitrogen adsorption. DSC measurements were performed with a Perkin-Elmer apparatus at a heating rate of 10 °C min^{-1} in air on 1.5 mg samples. SEM studies of the powders were carried out in a JEOL-5300 apparatus with an accelerating voltage of 25 kV.

The EPR spectra were recorded as a first derivative of the absorption signal with an ERS-220/Q (ex-GDR) spectrometer within the temperature range 90–400 K. The *g* factors were determined with respect to a Mn^{2+}/ZnS standard. The signal intensity was established by double integration of the experimental EPR spectrum.

3 Results

3.1 Lithium–manganese α-hydroxycarboxylate precursors

3.1.1 EPR of Mn^{2+} in lithium–manganese α-hydroxycarboxylate solutions. Complex formation in Li–Mn–organic acid solutions was explored by EPR spectroscopy of Mn^{2+} (Fig. 1). The EPR spectrum is a superposition of two signals with similar *g*-values ($g = 2.002$): one broad signal with a Lorentzian line shape and one well defined sextet [Fig. 1(a)]. The relative amount of the former increases as the solution concentration increases, but the line width remains nearly the same at *ca.* 44 mT (Fig. 1A). The mean line width of the sextet increases in the same way (inset in Fig. 1B). For the sake of comparison, Fig. 1(b) gives a typical EPR spectrum of the aqua-complex of manganese, $[Mn(H_2O)_6]^{2+}$, in $Mn(NO_3)_2$ aqueous solutions, as well as that of a freeze-dried $LiZn_2(cit)_2$ composition doped with 0.01% of Mn^{2+}. As one can see, the dependence of the mean line width of the sextet signal on the Mn^{2+} concentration is more pronounced for the organic acid solutions [inset in Fig. 1(b)]. The sextet signal for the concentrated Li–Mn–organic acid solutions resembles the sextet signal of Mn^{2+} dopants in the freeze-dried $LiZn_2(cit)_2$ composition [Fig. 1(b)].

3.1.2 Structure of freeze-dried lithium–manganese α-hydroxycarboxylate compositions. For Li–Mn–carboxylate compositions obtained by freeze-drying, only one broad Lorentzian with $g = 2.002$ gives rise to the EPR profile (Fig. 1A). The line width is slightly lower than that of the EPR signal of the corresponding solutions and varies between 34 and 38 mT: for mono-citrate and malate compositions, the line width is *ca.* 34 mT, while for bis-citrate composition the line width reaches 38 mT (Table 1).

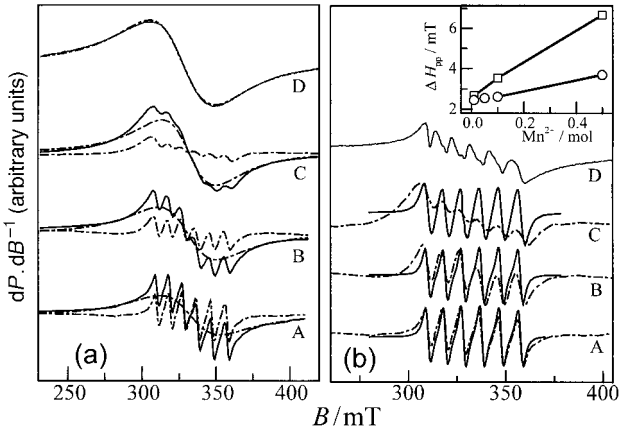

Fig. 1 (a) EPR spectra of Mn^{2+} in Li–Mn–citrate solutions with Mn : cit = 1 : 1 and 0.01 M Mn (A), 0.1 M Mn (B) and 0.5 M Mn (C). EPR spectrum of frozen Li–Mn–citrate solution with 0.1 M Mn (D). The solid lines correspond to the experimental spectra and dot–dashed lines to the deconvoluted spectra. (b) EPR spectra of Mn^{2+} in $Mn(NO_3)_2$ water solutions with 0.01 M Mn (A), 0.1 M Mn (B) and 0.5 M Mn (C). For the sake of comparison, dot–dashed lines show the deconvoluted sextet signal of Mn^{2+} in the Li–Mn–citrate solutions with the corresponding Mn concentration. EPR spectrum of Mn^{2+} ions diluted in a $LiZn_2(cit)_2$ freeze-dried composition (D). Inset gives the dependence of the mean EPR line width of the sextet signal of Mn^{2+} on the Mn concentration for $Mn(NO_3)_2$ (○) and Li-Mn-citrate (□) solutions.

In the spectral range between 1400 and 1600 cm^{-1}, the IR spectra of the freeze-dried compositions display the two bands characteristic for the asymmetric (ν_{as}) and symmetric (ν_s) stretching modes of the carboxylate group (Fig. 2). In addition, there is a splitting of ν_{as}- and ν_s-bands for mono-citrate and malate compositions (Table 1). With the exception of the bis-citrate composition, a weak band at *ca.* 1720 cm^{-1} superimposed on the ν_{as}-band can be resolved (Fig. 2). This weak band corresponds to the $\nu_{C=O}$ vibration of $^{-}CO_2H$ and reveals the presence of a small amount of free organic acid. As was mentioned in the Experimental section, the organic acid was dosed in over-stoichiometric amounts for the lactate, malate and mono-citrate compositions in order to obtain stable solutions in the pH range of 4.5–5.

The thermal properties of the lithium–manganese carboxylate compositions are compared in Fig. 3. For all samples, three regions can be distinguished in the DSC curves: (i) endothermic dehydration processes at 50–150 °C; (ii) endothermic processes due to transformation in the organic ligand at 150–220 °C, and (iii) strong exothermic processes occurring above 300 °C owing to the combustion of the organic residue. The temperature range where the exothermic process takes place depends on the kind of organic acid: the decomposition temperature increases from mono-citrate to bis-citrate *via* malate and lactate (Fig. 3 and Table 1). The exothermic effect of decomposition is, however, proportional to the number of carbon atoms: 74 ± 5 kcal per C atom.

3.2 Lithium–manganese spinels obtained from metal–organic precursors

3.2.1 Structure of ex-organic lithium–manganese spinels. Fig. 4 shows the X-ray patterns of lithium–manganese spinels obtained from the organic precursors. Irrespective of the organic acid, well crystallized lithium–manganese spinels appear already at 450 °C after a short heating time (5 h). However, the unit cell parameters are lower than that of standard $Li_{1.05}Mn_{1.95}O_4$ prepared by a solid phase reaction at

Table 1 EPR line width (ΔH_{pp}), asymmetric and symmetric stretching modes of CO_2^- (ν_{as} and ν_s) and decomposition temperatures (T_{max}), for freeze-dried Li–Mn–organic acid compositions

Compositions	ΔH_{pp}/mT	ν_{as}/cm^{-1}		ν_s/cm^{-1}		T_{max}/°C
$Li_{1.05}Mn_{1.95}(cit)_2{\cdot}xH_2O$	33.9±0.4	1620	1590	1397	1430	320
$Li_{1.05}Mn_{1.95}(mal)_3{\cdot}xH_2O$	33.9±0.2	1620	1580	1396	1420	385
$Li_{1.05}Mn_{1.95}(lac)_6{\cdot}xH_2O$	36.8±0.3	1590		1430		413
$Li_{1.05}Mn_{1.95}(cit)_4{\cdot}xH_2O$	38.0±0.4	1575		1405		437

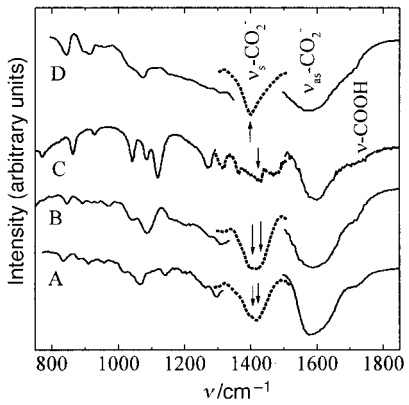

Fig. 2 IR spectra of freeze-dried $Li_{1.05}Mn_{1.95}(cit)_2$ (A), $Li_{1.05}Mn_{1.95}(mal)_3$ (B), $Li_{1.05}Mn_{1.95}(lac)_6$ (C) and $Li_{1.05}Mn_{1.95}(cit)_4$ (D). The solid and dotted lines correspond to the spectra registered in Nujol mulls and KBr pellets, respectively.

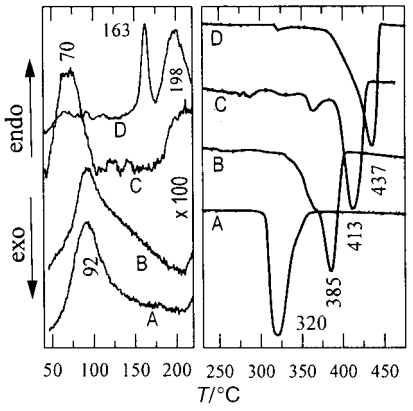

Fig. 3 DSC curves of freeze-dried $Li_{1.05}Mn_{1.95}(cit)_2$ (A), $Li_{1.05}Mn_{1.95}(mal)_3$ (B), $Li_{1.05}Mn_{1.95}(lac)_6$ (C) and $Li_{1.05}Mn_{1.95}(cit)_4$ (D).

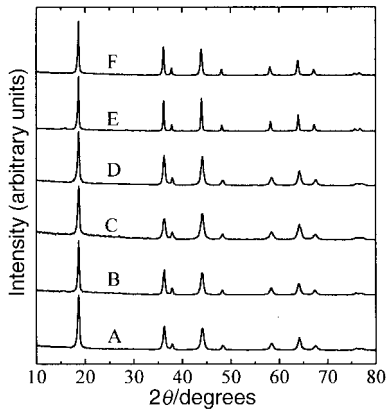

Fig. 4 XRD patterns of lithium–manganese spinels obtained at 450 °C from mono-citrate (A), malate (B), lactate (C) and bis-citrate (D) precursors. For the sake of comparison, XRD patterns of the ex-lactate spinel annealed at 750 °C (E) and of the spinel obtained by solid state reaction (F) are also given.

750 °C (Table 2). In addition, the decrease in the unit cell parameters of ex-organic spinels is associated with a linear increase in the mean oxidation state of the manganese ions (Fig. 5). This dependence is not obeyed for the samples annealed at 750 °C: small changes in the oxidation state of manganese result in significant increase in the unit cell parameters (Fig. 5). At the same time, the composition and the structure of the annealed spinels are sensitive towards the type of the organic acid used for the precursors (Table 2).

For annealed spinels, the unit cell parameters and the mean oxidation state of Mn depend on the temperature of the sample quenching (Fig. 6). The samples quenched from 750 °C are characterized by higher unit cell parameters and, correspondingly, with lower mean oxidation state of Mn as compared with slow cooled samples (Fig. 6). At a lower temperature of sample quenching, the structure and composition of the ex-organic spinels reach these for standard $Li_{1.05}Mn_{1.95}O_4$ (Fig. 6). This quenching temperature is sensitive to the sample nature (Fig. 6): 590 and 880 K (320 and 610 °C) for ex-lactate and ex-bis citrate spinels, respectively.

3.2.2 EPR of ex-organic lithium–manganese spinels. Fig. 7 compares the EPR spectra of ex-organic spinels with those of standard $Li_{1.05}Mn_{1.95}O_4$. The EPR spectra of the spinels display several signals: an intense signal with Lorentzian shape and additional low-intensity signals with positions and shapes depending on the spinel histories. The main Lorentzian signal with $g=2.02$ is found in the spectra of all samples investigated (Fig. 7). The temperature dependence of the signal intensity does not obey the Curie–Weiss law: on cooling, the intensity increases and but then drops at $T<220$ K (Fig. 8). This drop is different for spinels obtained at 450 °C and those annealed at 750 °C (Fig. 8). The Lorentzian line width increases with decreasing temperature (Fig. 9). This dependence is more pronounced with slow cooled high-temperature samples. Only with samples quenched from 750 °C does the line width show a complex temperature dependence: ΔH_{pp} increases on cooling and decreases below 220 K (Fig. 9). For slow cooled spinels,

Table 2 Unit cell parameters (a), mean oxidation state of Mn (m), and oxygen non-stoichiometry (γ), for ex-lactate and ex-bis citrate spinels obtained at 450 °C with a heating rate of 1 °C min^{-1}, annealed at 750 °C and slow cooled to room temperature (750 °C–s.c.), and annealed at 750 °C and metal quenched from: 750 °C (750 °C–m.q.); 600 °C (600 °C–m.q.); and 500 °C (500 °C–m.q.). As a comparison, data for $Li_{1.05}Mn_{1.95}O_4$ obtained by solid state reaction are also included

	Condition	a/Å[a]	m[b]	γ[c]
Lactate	450 °C	8.2082	3.622	0.056
	750 °C–s.c.	8.2305	3.577	0.013
	500 °C–m.q.	8.2342	3.554	−0.010
	600 °C–m.q.	8.2393	3.541	−0.023
	750 °C–m.q.	8.2423	3.535	−0.028
Bis-citrate	450 °C	8.2093	3.620	0.054
	750 °C–s.c.	8.2174	3.614	0.049
	600 °C–m.q.	8.2294	3.560	−0.004
	750 °C–m.q.	8.2368	3.549	−0.015
$Li_{1.05}Mn_{2.05}O_4$	750 °C–s.c.	8.2328	3.565	0.000
$Li_{1.05}Mn_{2.05}O_4$	750 °C–m.q.	8.2402	3.533	−0.030

[a] ±0.0003 Å. [b] ±0.004. [c] γ in $Li_{1.05}Mn_{1.95}O_{4+\gamma}$.

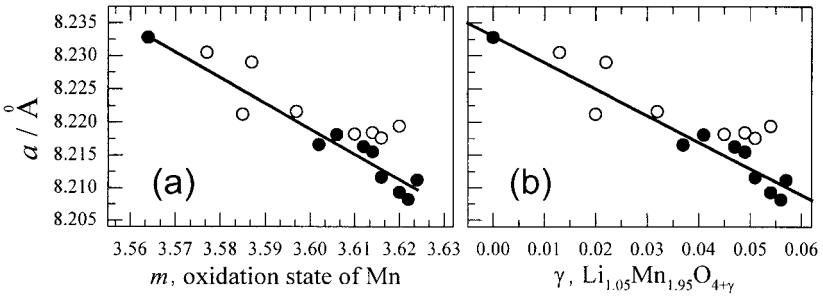

Fig. 5 Unit cell parameters of ex-organic spinels obtained at 450 °C (●) and annealed at 750 °C (○) as a function of the oxidation state of Mn (a) and of the oxygen non-stoichiometry (b).

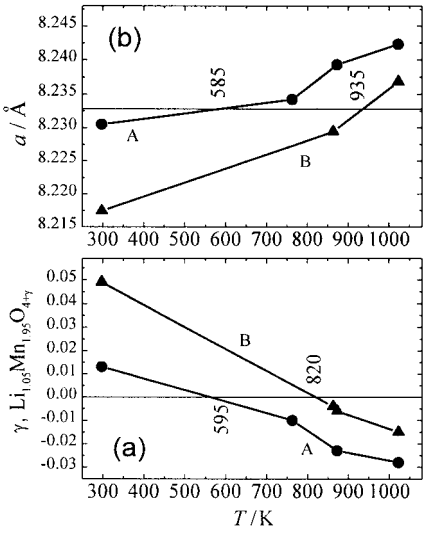

Fig. 6 Oxygen non-stoichiometry (a) and unit cell parameters (b) as a function of the quenching temperature for ex-lactate (●) and ex-bis-citrate (▲) spinels.

the temperature dependences of the line width and the signal intensity are close to those of standard $Li_{1.05}Mn_{1.95}O_4$.

The most characteristic feature of the EPR spectra of ex-organic spinels is the appearance of two low-intensity signals with Lorentzian shape and $g=2.001$ and 1.998, respectively (Fig. 7). These signals are not observed in the EPR spectrum of standard $Li_{1.05}Mn_{1.95}O_4$ obtained by solid state reaction (Fig. 7). With all samples investigated, the temperature dependence of the intensity of the broader additional signal ($g=2.001$) follows the Curie–Weiss law, the Weiss constant being 20 K. On heating, the line width decreases and reaches its minimum value of *ca.* 85 mT at 413 K (Fig. 10). The intensity of the additional broader signal is up to 2% of the main Lorentzian for the low-temperature ex-organic spinels and increases significantly for the samples annealed at 750 °C. Moreover, the relative intensity of this signal depends on the sample history (Table 3): the intensity varies between 6 and 12% for the lactate and bis-citrate precursors, respectively. The additional narrower signal ($g=1.998$ and relative intensity *ca.* 1%) is observed only with the annealed ex-lactate spinels. The Weiss constant for this signal is 30 K and the line width increases on heating. The line width is *ca.* 20 mT at 413 K (Fig. 10).

Quenching the spinels from 750 °C leads to the appearance of another additional signal, however, with a Gaussian line shape [Fig. 7(c)]. The *g* factor increases from 2.5 to 4 on cooling. In addition, the appearance of the Gaussian signal only depends on the cooling rate and not on the nature of the organic precursor. In contrast to the additional Lorentzians, the signal with the Gaussian shape is observed in the EPR spectrum of standard $Li_{1.05}Mn_{1.95}O_4$. This signal has been recently attributed to complex associates of defects including manganese in a low-symmetry crystal field and oxygen vacancies.[38]

No additional EPR signals are visible in the spectra of ex-organic spinels quenched from lower temperatures (500 and 600 °C) for ex-lactate and bis-citrate compositions,

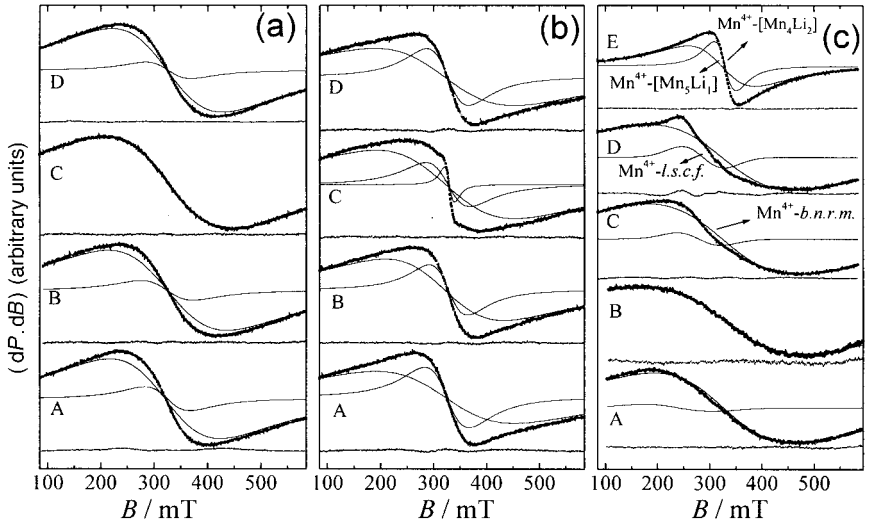

Fig. 7 (a) EPR spectra at 413K of ex-mono-citrate (A), ex-malate (B), ex-lactate (C) and ex-bis-citrate (D) spinels obtained at 450 °C. (b) EPR spectra at 413 K of ex-mono-citrate (A), ex-malate (B), ex-lactate (C) and ex-bis-citrate (D) spinels annealed at 750 °C. (c) EPR spectra at 413 K of ex-lactate spinels quenched from 750 °C (A) and 500 °C (B), slow cooled (C) and metal quenched (D) $Li_{1.05}Mn_{1.95}O_4$ obtained by solid state reaction and $Li[Li_{1/3}Mn_{5/3}]O_4$ obtained at 450 °C (E). Dotted lines correspond to the experimental spectra, while the solid thin lines represent the deconvoluted spectra. The main Lorentzian and the additional Gaussian are denoted as Mn^{4+}-b.n.r.m. and Mn^{4+}-l.s.c.f. respectively.

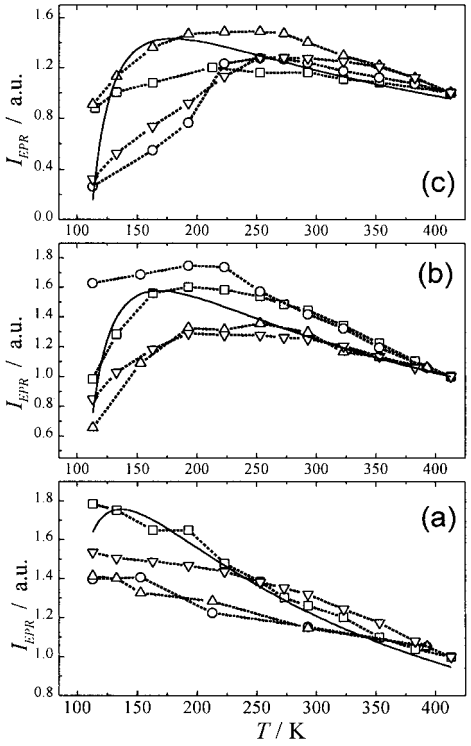

Fig. 8 Temperature variation of the intensity of the main EPR signal for ex-mono-citrate (□), ex-malate (○), ex-lactate (△) and ex-bis-citrate (▽) spinels obtained at 450 °C (a) and annealed at 750 °C (b). (c) Temperature variation of the EPR intensity for ex-lactate spinel quenched from 600 (□) and 750 °C (○) and for ex-bis-citrate spinel quenched from 600 (△) and 750 °C (▽). For the sake of comparison, the solid lines represent the temperature variation of the EPR intensity of the main EPR signal for slow cooled $Li_{1.1}Mn_{1.9}O_4$ (a), slow cooled $Li_{1.05}Mn_{1.95}O_4$ (b) and metal quenched $LiMn_2O_4$ (c) obtained by solid state reaction.

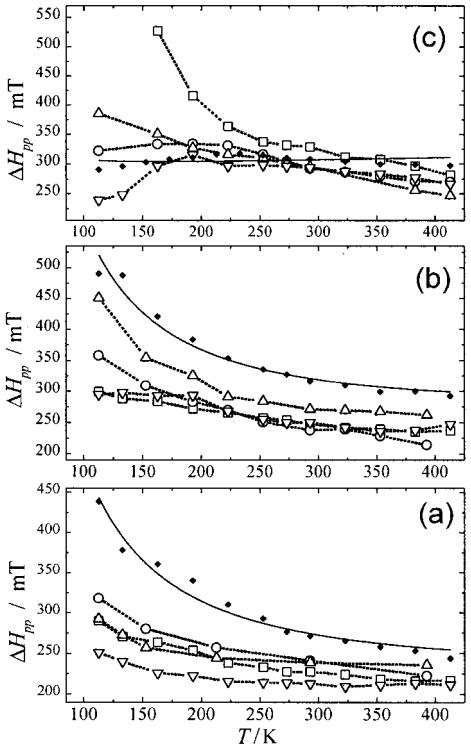

Fig. 9 Temperature variation of the EPR line width of the main signal for ex-mono-citrate (□), ex-malate (○), ex-lactate (△) and ex-bis-citrate (▽) spinels obtained at 450 °C (a) and annealed at 750 °C (b). (c) Temperature variation of the EPR line width for ex-lactate spinel quenched from 600 (□) and 750 °C (○) and for ex-bis-citrate spinel quenched from 600 (△) and 750 °C (▽). For the sake of comparison, the solid lines and ◆ symbols represent the temperature variation of the EPR line width for slow cooled $Li_{1.1}Mn_{1.9}O_4$ (a), slow cooled $Li_{1.05}Mn_{1.95}O_4$ (b) and metal quenched $LiMn_2O_4$ (c) obtained by solid state reaction.

respectively. Only the intense Lorentzian described above gives rise to the EPR spectrum in this case (Fig. 7).

Summarizing, the EPR signals observed in ex-organic lithium–manganese spinels can be divided into three groups:

(i) a main EPR signal with a Lorentzian shape and $g = 2.02$ observed for all samples, regardless of the temperature of preparation and quenching.

(ii) An additional EPR signal with a Lorentzian shape ($g = 2.001$), a line width of *ca.* 80 mT and a relative intensity of *ca.* 6–12% observed for the spinels slow cooled from 750 °C; a second low-intensity Lorentzian with an intensity of *ca.* 1% and with $g = 1.998$ and a smaller line width (*ca.* 20–30 mT) characteristic of annealed ex-lactate spinels only.

(iii) An EPR signal with a Gaussian shape appearing for spinels quenched from 750 °C.

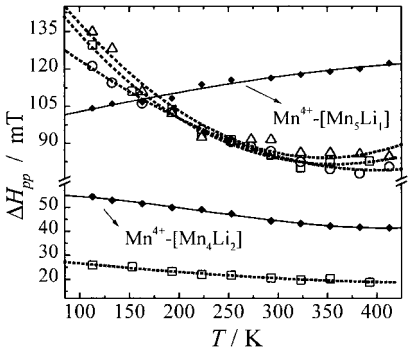

Fig. 10 Temperature variation of the EPR line width of the additional Lorentzian signals for ex-bis citrate spinel obtained at 450 °C (△) and for ex-lactate (□) and ex-bis-citrate (○) spinels annealed at 750 °C. For the sake of comparison, the solid lines and ◆ symbols represent the temperature variation of the EPR line width of the two signals for $Li[Li_{1/3}Mn_{5/3}]O_4$ obtained by solid state reaction.

4 Discussion

To take advantage of low-temperature synthesis techniques, the initial components should be mixed on an atomic level. In this connection, the use of α-hydroxycarboxylate acids as chelating ligands with hydroxy and carboxylate groups permits chemical design of the precursors. In our case, EPR spectroscopy of Mn^{2+} provides an opportunity to explore the complexation processes in Li–Mn–α-hydroxycarboxylate solutions and in the corresponding freeze-dried compositions. Since the Mn^{2+} ions are in a singlet orbital state ($^6S_{5/2}$), one should expect that complex formation in the solution would cause broadening of the EPR line due to suppression of the chaotic motion of Mn^{2+} species. This means that the EPR line width is sensitive to complex formation in solution. As one can expect, the typical sextet of the aqua-complex of manganese is broadened in solutions containing α-hydroxyorganic acids, culminating in the appearance of one broad Lorentzian with a line width of *ca.* 40 mT (Fig. 1). This means that Mn^{2+} ions form isolated complexes with α-hydroxyorganic acids in solution, on the one hand, and that these complexes are associated into polymeric units, on the other. Polynuclear Mn^{2+}–organic acid complexes also appear in dilute solutions containing a significant amount of $[Mn(H_2O)_6]^{2+}$.

During freeze-drying of the solutions, polynuclear Mn–organic acid complexes are formed at the expense of $[Mn(H_2O)_6]^{2+}$ and isolated Mn^{2+}–organic acid complexes.

Table 3 Relative intensity of the additional Lorentzian signal $[I/(I_{b.n.r.m.}+I)]$, total amount of lithium (y_{tot}), and of metal vacancies (δ_{tot}), total oxygen non-stoichiometry (γ_{tot}), calculated amount of lithium (y_{vol}), and of metal vacancies (δ_{vol}), in the spinel bulk, and relative fraction of the Mn^{4+}-rich surface layer (s), for ex-organic $Li[Li_yMn_{2-y-\delta}\square_\delta]O_4$ spinels obtained at 450 °C with a heating rate of 1 °C min^{-1} and annealed at 750 °C and slow cooled to room temperature

Composition	$I/(I_{b.n.r.m.}+I)$ (%)	y_{exp}	δ_{exp}	γ_{exp}	y_{vol}	δ_{vol}	s (%)
Ex-$(cit)_2$–450 °C	1.2	0.037	0.038	0.051	—	—	—
Ex-$(mal)_3$–450 °C	2.3	0.040	0.028	0.037	—	—	—
Ex-$(lac)_6$–450 °C	—	0.035	0.042	0.056	—	—	—
Ex-$(cit)_4$–450 °C	1.9	0.036	0.040	0.054	—	—	—
Ex-$(cit)_2$–750 °C	11.7	0.036	0.040	0.054	0.041	0.027	4.75
Ex-$(mal)_3$–750 °C	7.1	0.044	0.017	0.022	0.047	0.010	2.26
Ex-$(lac)_6$–750 °C	6.0	0.047	0.010	0.013	0.048	0.004	1.64
Ex-$(cit)_4$–750 °C	8.5	0.037	0.036	0.049	0.040	0.029	2.54

Finally, amorphous whitish powders with compositions $LiMn_2(lac)_6{\cdot}xH_2O$, $LiMn_2(mal)_3{\cdot}xH_2O$, $LiMn_2(cit)_2{\cdot}xH_2O$ and $LiMn_2(cit)_4{\cdot}xH_2O$ ($x=2$–4) are formed. The coordination of the organic acids to Mn^{2+} through carboxylic groups is manifested in the IR spectra of the precursors, where the asymmetric and symmetric stretching modes of the carboxylate groups grow in intensity as compared to that of the protonated $-CO_2H$ groups (Fig. 2). In addition, the asymmetric and symmetric stretching frequencies, as well as the differences between them, reflect the mode of the carboxylate coordination to Mn^{2+}. For mono-citrate and malate compositions, the doubling of the two frequencies (ν_{as} and ν_s) indicates at least two modes of CO_2^- coordination, while for the lactate and bis-citrate compositions one mode of carboxylate coordination prevails (Table 1). This result is in good agreement with crystal structure data on the α-hydroxycarboxylate salts of transition metals.

Taking into account the crystal structure data on α-hydroxycarboxylate coordination to transition metal ions, it is convenient to differentiate the α-hydroxycarboxylate salts of transition metals in terms of monomeric and polymeric complexes. For the Zn/Mn–lactate[40,41] and Zn/Cu–bis-citrate[42,43] compositions, the metal ions form distinct complexes with two lactate and two citrate ions, respectively, the crystal structure being stabilized by strong hydrogen bonding. For Mn–mono-citrates[44] and Mn–malates,[45] β-carboxyl groups bridge the metal ion complexes into infinite chains. The formation of discrete or polymeric complexes can be used to rationalise the EPR line width of Mn^{2+} in the freeze-dried $LiMn_2$–α-hydroxy-carboxylate precursors. As is well known, the EPR line width in magnetically concentrated systems is a result from dipole–dipole and exchange interactions. Since the Mn^{2+}–Mn^{2+} distances in the α-hydroxycarboxylate salts are similar, then the dipole–dipole interactions would have almost the same effect on the EPR line width of Mn^{2+}. By contrast, the exchange coupling between Mn^{2+} would be more effective for the structures containing infinite Mn^{2+}-chains. As a result, the EPR line width of Mn^{2+} in mono-citrate and malate compositions would be lower as compared to that of the lactate and bis-citrate compositions. This is the order that we have observed for the EPR line width of the freeze-dried $LiMn_2$ α-hydroxycarboxylate compositions (Table 1).

Summarizing, the EPR and IR data suggest that in the amorphous carboxylate precursors obtained by freeze-drying the coordination of Mn^{2+} does not differ from that in the crystalline analogues. Considering the nature of the α-hydroxyorganic acid coordination to the transition metal ions,[40–45] the first coordination sphere of Mn^{2+} in freeze-dried compositions can be presented as follows:

(i) with lactic acid: $[MnO_2^{CO_2^-}O_2^{OH}O_2^{H_2O}]$

(ii) with malic acid: $[MnO_3^{CO_2^-}O_1^{OH}O_2^{H_2O}]^-$

(iii) with 1 mol citric acid: $[MnO_4^{CO_2^-}O_1^{OH}O_1^{H_2O}]^{2-}$

(iv) with 2 mol citric acid: $[MnO_4^{CO_2^-}O_2^{OH}]^{4-}$

The thermal properties of the lithium–manganese organic compositions reflect their different structure: the decomposition temperature is lower for mono-citrate and malate compositions where polymeric structural units are developed (Fig. 3 and Table 1).

At 450 °C, the thermal decomposition of metal–organic precursors yields lithium–manganese spinels, in which the amount of Mn^{4+} is in excess of the stoichiometric value. In the literature, spinels rich in Mn^{4+} are often denoted as defect spinels.[37] With these defect spinels, the charge compensation is achieved by creation of metal vacancies. According to the Li–Mn–O phase diagram proposed by Xia and Yoshio,[46] cation vacancies can be present on the octahedral or on both tetrahedral and octahedral sites:

$$(Li)_{8a}[Mn_{8/(n+m)}Li_{(7n-m)/(n+m)}\square_{(3m-5n-8)/(n+m)}]_{16d}O_4,\quad m/7\leqslant n\leqslant(3m-8)/5,\ 3.5\leqslant m\leqslant 4.0 \qquad (1)$$

$$(Li_{8n/(n+m)}\square_{(m-7n)/(n+m)})_{8a}[Mn_{8/(n+m)}\square_{(2n+2m-8)/(n+m)}]_{16d}O_4,\quad 0.5\leqslant n\leqslant m/7,\ 3.5\leqslant m\leqslant 4.0 \qquad (2)$$

where the Li/Mn molar ratio and the mean oxidation state of Mn are represented by n and m, respectively, and the symbol $\square$ represents a cation vacancy.

For the Mn^{4+} -rich ex-organic spinels with a Li/Mn molar ratio of 0.538 and a mean oxidation state of manganese varying between 3.56 and 3.62, the cation distribution should be presented by formula (1), *i.e.* by cation vacancies on the octahedral sites only. Table 3 gives the calculated amount of lithium (y), and metal vacancies (δ) in the octahedral sublattice. (We shall note that the attempts to introduce vacancies into the tetrahedral spinel positions do not agree with the chemical analysis data.) For the sake of comparison, the same Table presents the calculated amount of excess oxygen per spinel formula unit, $Li[Li_xMn_{2-x}]O_{4+y}$. The linear correlation between the amount of the excess Mn^{4+} and the unit cell parameter points to a uniform distribution of the vacancies in the octahedral positions of low-temperature spinels (Fig. 6). The ex-lactate and ex-malate spinels annealed at 750 °C display a trend to decreasing the metal vacancies as compared to the low-temperature analogues, while the ex-mono- and ex-bis-citrate spinels exhibit only negligible changes in composition. In addition, the disturbance of the linear correlation between the amount of Mn^{4+} and the unit cell parameters evidences peculiarities in the cation distribution of the spinels annealed at 750 °C.

In order to monitor the cation distribution in the lithium–manganese spinels, we have used EPR of Mn^{4+} ions. As was shown recently, the EPR signal in a magneto-concentrated system such as the spinel $Li_{1+x}Mn_{2-x}O_4$ ($0\leqslant x\leqslant 0.1$) may be interpreted within the framework of the bottle-neck relaxation mechanism (b.n.r.m.).[38] According to this mechanism, the direct relaxation of Mn^{4+} is not effective enough for disturbing the collective motion of the total magnetic moment of the Mn^{3+} and Mn^{4+} spin system. This relaxation mechanism

determines the temperature dependence of the signal intensity and the line width, which is sensitive to the Mn^{3+}/Mn^{4+} ratio. For all ex-organic spinels, the main Lorentzian signal with $g=2.02$ has the characteristic features of the bottle-neck relaxation mechanism. With ex-organic spinels obtained at 450 °C, the higher amount of Mn^{4+} leads to a temperature dependence of the EPR line width and of the signal intensity that do not match that of stoichiometric $Li_{1.05}Mn_{1.95}O_4$ (Fig. 8 and 9). Irrespective of this, the bottle-neck relaxation mechanism still operates. This result confirms the uniform distribution of excess Mn^{4+} ions (and the corresponding metal vacancies) in the bulk of low-temperature spinels. By contrast, for spinels annealed at 750 °C, the parameters of the main EPR signal approach those of stoichiometric $Li_{1.05}Mn_{1.95}O_4$, especially in the case of ex-lactate and ex-malate spinels (Fig. 8 and 9). This EPR result and the increased unit cell parameters appear to contradict the chemical analysis data. However, this apparent contradiction may be resolved by considering the EPR data with respect to the additional low-intensity EPR signals in ex-organic spinels [Fig. 7(b)].

In contrast to the main EPR signal, the additional signal with $g=2.001$ and $\Delta H_{pp}\approx 80$ mT has the characteristic features of exchange-coupled paramagnetic particles: the EPR line has a Lorentzian shape and its intensity varies with temperature, following the Curie–Weiss law. These parameters allow this additional signal to be attributed to exchange-coupled Mn^{4+} ions. The amount of these ions as estimated from the signal intensity at 413 K varies between 5 and 15%. In addition, only ex-lactate spinels produce an additional Lorentzian with $g=1.998$, $\Delta H_{pp}\approx 25$ mT and a relative intensity of up to 1% [Fig. 7(b)]. Evidently, the narrow signal can also be ascribed to Mn^{4+}. With a view to more detailed description of these signals, the EPR spectra of ex-organic spinels are compared with the EPR spectrum of the $Li[Li_{1/3}Mn_{5/3}]O_4$ spinel containing Mn^{4+} only in Fig. 7(c). The EPR spectrum of $Li[Li_{1/3}Mn_{5/3}]O_4$ contains two overlapping signals with Lorentzian shapes and different line widths. Similarly, the parameters of these signals match the parameters of the two additional Lorentzians in ex-organic spinels. On the basis of line width analysis in terms of dipole–dipole and exchange interactions, we have recently assigned these two signals to two types of Mn^{4+}.[37] The broader signal corresponds to Mn^{4+} whose first coordination sphere includes $5Mn^{4+}$ and $1Li^+$ ions, while the Mn^{4+} ions in an environment rich in Li^+ produce the narrower signal.[37] Returning to the ex-organic spinels, it seems that the two additional Lorentzians can also be attributed to two types of Mn^{4+}: with a Mn^{4+}-rich shell (the broader signal) and with a Li^+-rich shell (the narrower signal).

The appearance of additional EPR signals in the spectra of ex-organic spinels annealed at 750 °C implies a non-uniform distribution of Mn^{4+}. The simultaneous registration of the main and the two additional signals is an indication that the exchange-coupled Mn^{4+} ions are magnetically isolated from the main Mn^{3+}–Mn^{4+} spin system. The similar parameters of the main EPR signal for the ex-organic spinels and for stoichiometric $Li_{1.05}Mn_{1.95}O_4$ suggest that the bulk of the ex-organic spinels and the stoichiometric spinel are similar in composition, whereas the surface accommodates the excess Mn^{4+}. This is a phenomenon known to occur for spinels. Thus, with the normal cobalt spinel, Co_3O_4, an oxygen-rich surface layer is formed, which determines the catalytic and electrocatalytic properties.[47,48] Irrespective of the fact that the intercalation properties belong to the bulk, the formation of Mn^{4+} rich surface layers would affect lithium transport in lithium–manganese spinels.

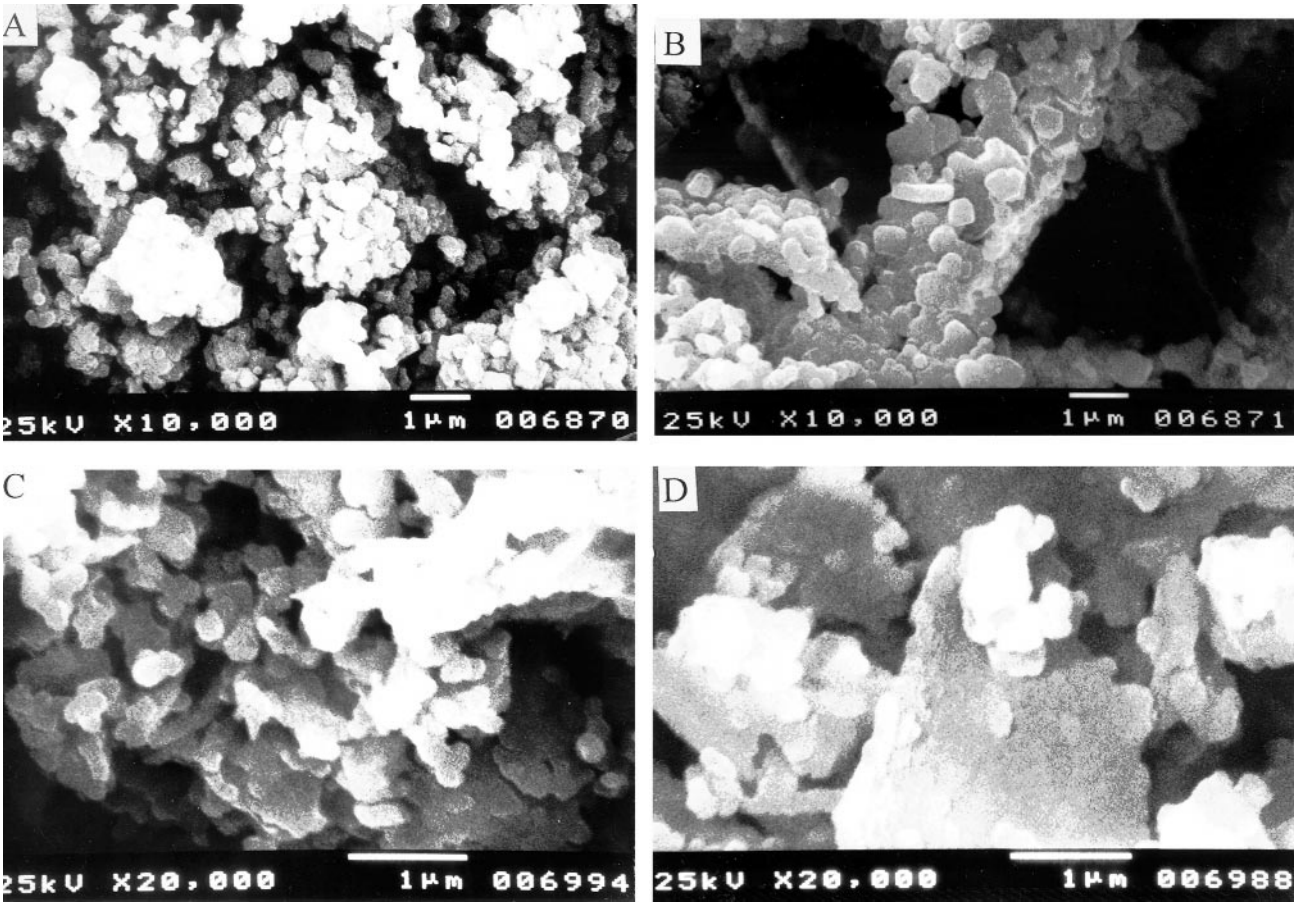

Fig. 11 SEM micrographs of $LiMn_2O_4$ obtained at 750 °C from: γ-MnO_2 and Li_2CO_3 (A), lactate (B), mono-citrate (C) and bis-citrate precursors (D).

For the annealed samples, the non-uniform distribution of excess Mn^{4+} perturbs the linear correlation between the unit cell parameter and the amount of excess Mn^{4+}. At the same time, it is possible to use this linear correlation observed with low-temperature spinels for the evaluation of the bulk composition of the high-temperature spinels (Table 3). As was to be expected, the bulk composition of the high-temperature spinels tends to that of stoichiometric $Li_{1.05}Mn_{1.95}O_4$. The largest deviations from the stoichiometric composition are observed with ex-citrate spinels. This is in accord with the temperature dependence of the line width of the main EPR signal [Fig. 9(b)]. Assuming the presence of Mn^{4+} only in the surface regions and absence of a gradient of lithium within the spinel particles, one may determine the relative fraction of these Mn^{4+}-rich surface regions from the data of chemical analysis and the bulk composition (Table 3). As one can see, the relative fraction of the Mn^{4+}-rich regions is sensitive to the organic precursor used: Mn^{4+}-rich surface regions are developed to a greater extent in spinels obtained from citrate precursors. This is probably due to the different morphologies of the spinel particles: on the SEM micrographs well shaped crystallites of *ca.* 500 nm are clearly visible with ex-lactate spinels whereas for the citrate precursors there are agglomerates of spinel particles (Fig. 11).

Attempting to check this model, EPR data on the additional low-intensity signals were used. Since these signals reflect formation of the Mn^{4+}-rich regions, their relative intensities will give the relative fraction of Mn^{4+} in the surface regions. The correlation between the relative fraction of the Mn^{4+}-rich surface regions (calculated from chemical analysis and XRD data) and the intensity of the additional Lorentzian signal with $H_{pp} \approx 80$ mT is given in Fig. 12. The linear correlation observed confirms the suitability of the model for the non-uniform distribution of Mn^{4+} in ex-organic high-temperature spinels.

Recently, lithium–manganese spinels have been shown to be thermally unstable: between 700 and 950 °C, $Li_{1+x}Mn_{2-x}O_4$ spinels show reversible weight loss owing to oxygen intercalation and deintercalation reactions.[30,31] Oxygen evolution is accompanied by formation of complex associates of defects including several Mn^{3+} and oxygen vacancies.[14] With ex-organic spinels quenched from 750 °C, there is a simultaneous increase of the unit cell parameter and a decrease of the mean oxidation state of the manganese ions (Table 2). Moreover, the oxygen loss leads to a similar composition and structure of ex-organic spinels (Fig. 6). This is accompanied by a corresponding change of the EPR spectra: the temperature dependence of the line width of the main EPR signal is similar to that of stoichiometric $Li[Mn_2]O_4$, but differs from that of $Li[Li_{0.05}Mn_{1.95}]O_4$ [Fig. 9(c)]. This result reflects changes in the bulk composition of the quenched high-temperature spinels and suggests a uniform distribution of the temperature-generated Mn^{3+} ions in the spinel lattice. As was pointed out above, the signal indicating the formation of complex defect associates of Mn and oxygen vacancies is the Gaussian. This signal is observed in the spectrum of quenched $Li[Li_{0.05}Mn_{1.95}]O_4$ obtained by solid state reaction as well as in very small amounts in the spectrum of slow cooled stoichiometric $Li[Li_{0.05}Mn_{1.95}]O_4$. With ex-organic spinels, the Gaussian signal is observed in samples quenched from 750 °C only.

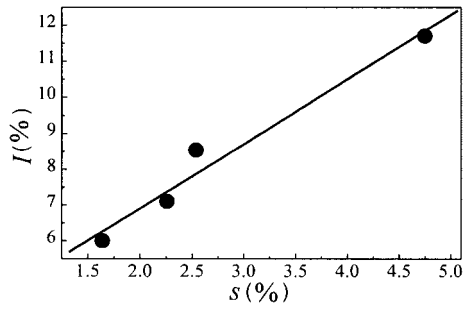

Fig. 12 Correlation between the relative EPR intensity for the additional Lorentzian signal, *I*, and the relative fraction of the Mn^{4+}-rich surface regions, *s*.

The ability of spinels to exchange oxygen with the environment during cooling should also be taken into account. With a decrease of the quenching temperature, the composition, structure, and EPR spectra of the spinels change again: the mean oxidation state of manganese ions increases, the unit cell parameter decreases (Table 2) and the temperature dependence of the line width is similar to that of stoichiometric $Li[Li_{0.05}Mn_{1.95}]O_4$ (Fig. 9), which is an indication for annihilation of Mn^{3+} ions that appeared at 750 °C. At the same time, the Gaussian and the additional Lorentzians are not registered in the EPR spectra of the spinels quenched at lower temperatures (600 and 500 °C for the bis-citrate and lactate composition, respectively). This means that at these quenching temperatures the ex-organic spinels tend to the stoichiometric $Li[Li_{0.05}Mn_{1.95}]O_4$. In addition, the temperature at which ex-organic spinels acquire the composition and structure of the 'standard' $Li[Li_{0.05}Mn_{1.95}]O_4$, depends on the type of the lithium-manganese organic precursor. The different reactivity of the lithium–manganese spinel oxides in the oxygen loss/uptake reactions is, most probably, a result of the different morphology of the powdered samples.

5 Conclusions

The thermal decomposition of metal–organic precursors at low temperatures (450 °C) yields $Li[Li_yM_{2-y-\delta}\square_\delta]O_4$ spinels, in which excess Mn^{4+} and corresponding vacancies are randomly distributed. Additional annealing at 750 °C leads to a removal of the excess Mn^{4+} from the bulk of the spinel, as a result of which the bulk becomes close to the stoichiometric composition. The spinel surface is able to uptake oxygen during cooling, thus accommodating excess Mn^{4+} ions. The formation of Mn^{4+}-rich surface regions depends not only on the cooling rate but also on the sample morphology, which is a result of the type of the lithium–manganese organic precursor. Lactate precursors produce spinels less susceptible for oxygen uptake reactions as compared to citrate precursors.

Acknowledgements

Financial support from the National Science Fund of Bulgaria (Contract no. Ch810/1998) is gratefully acknowledged.

References

1 M. M. Thackeray, *Prog. Batteries Batteries Mater.*, 1992, **11**, 150.
2 R. Koksbang, J. Barker, H. Shi and M. Y. Saïdi, *Solid State Ionics*, 1996, **84**, 1.
3 P. G. Bruce, *Chem. Commun.*, 1997, 1817.
4 J. M. Tarascon, *US Pat.*, 1996, **6**, 295.
5 R. J. Gummow, A. de Kock and M. M. Thackeray, *Solid State Ionics*, 1994, **69**, 59.
6 J. M. Tarascon, W. R. McKinnon, F. Coowar, T. N. Bowmer, G. Amatucci and D. Guyomard, *J. Electrochem. Soc.*, 1994, **141**, 1421.
7 Y. Gao and J. R. Dahn, *J. Electrochem. Soc.*, 1996, **143**, 100.
8 D. G. Wickham and W. Groft, *J. Phys. Chem. Solids*, 1958, **7**, 351.
9 F. le Cras, P. Strobel, M. Anne, D. Bloch, J.-B. Soupart and J.-C. Rousche, *Eur. J. Solid State Chem.*, 1996, **33**, 67.
10 M. M. Thackeray, A. de Kock and W. I. F. David, *Mater. Res. Bull.*, 1993, **28**, 1041.
11 T. Takada, H. Hayakawa and E. Akiba, *J. Solid State Chem.*, 1995, **115**, 420.
12 A. de Kock, M. H. Rossouw, L. A. de Picciotto, M. M. Thackeray, W. I. F. David and R. M. Ibberson, *Mater. Res. Bull.*, 1990, **25**, 657.
13 A. Yamada, K. Miura, K. Hinokuma and M. Tanaka, *J. Electrochem. Soc.*, 1995, **142**, 2149.

14 J. Sugiyama, T. Atsumi, T. Hioki, S. Noda and N. Kamegashira, *J. Alloys Compd.*, 1996, **235**, 163.
15 M. M. Thackeray, *J. Electrochem. Soc.*, 1997, **144**, L100.
16 M. M. Thackeray, Y. Shao-Horn, A. J. Kahaiana, K. D. Kepler, E. Skinner, J. T. Vaughey and S. A. Hackney, *Electrochem. Solid-State Lett.*, 1998, **1**, 7.
17 P. Barboux, J. M. Tarascon and F. K. Shokoohi, *J. Solid State Chem.*, 1991, **94**, 185.
18 P. G. Bruce, *Phil. Trans. R. Soc. London Sect. A*, 1996, 1577.
19 T. Tsumura, S. Kishi, H. Konno, A. Shimizu and M. Inagaki, *Thermochim. Acta*, 1996, **278**, 135.
20 T. Tsumura, A. Shimizu and M. Inagaki, *J. Mater. Chem.*, 1993, **3**, 995.
21 S. R. S. Prabaharan, M. S. Michael, T. P. Kumar, A. Mani, K. Athinarayanaswamy and R. Gangadharan, *J. Mater. Chem.*, 1995, **5**, 1035.
22 H. Yasushi (Nippondenso Co., Ltd.), *US Pat.*, 5 565 688, Oct. 15, 1996.
23 W. Liu, G. C. Farrington, F. Chaput and B. Dunn, *J. Electrochem. Soc.*, 1996, **143**, 879.
24 L. Hernán, J. Morales, L. Sánchez and J. Santos, *Solid State Ionics*, 1997, **104**, 205.
25 P. Fragnaud and D. M. Schleich, *Sens. Actuators A*, 1995, **51**, 21.
26 P. Fragnaud, R. Nagarajan, D. M. Schleich and D. Vujic, *J. Power Sources*, 1995, **54**, 362.
27 Y.-K. Sun, *Solid State Ionics*, 1997, **100**, 115.
28 J. N. Reimers, E. W. Fuller, E. Rossen and J. R. Dahn, *J. Electrochem. Soc.*, 1993, **140**, 3396.
29 I. Kotschou, M. N. Richard, J. R. Dahn, J. B. Soupart and J. C. Rousche, *J. Electrochem. Soc.*, 1995, **142**, 2906.
30 A. R. Armstrong and P. G. Bruce, *Nature*, 1996, **381**, 499.
31 M. M. Thackeray, *J. Electrochem. Soc.*, 1995, **142**, 2558.
32 C. Fong, J. B. Kennedy and M. M. Elcombe, *Z. Kristallogr.*, 1994, **209**, 941.
33 V. Massarotti, M. Bini and D. Capsoni, *Z. Naturforsch.*, *Teil A*, 1996, **51**, 267.
34 Y. Gao and J. R. Dahn, *Appl. Phys. Lett.*, 1995, **66**, 2487.
35 M. M. Thackeray, M. F. Mansuetto, D. W. Dees and D. R. Vissers, *Mater. Res. Bull.*, 1996, **31**, 133.
36 V. Massarotti, D. Capsoni, M. Bini and C. B. Azzoni, *J. Solid State Chem.*, 1997, **128**, 80.
37 R. Stoyanova, M. Gorova and E. Zhecheva, *J. Phys. Chem. Solids*, submitted.
38 R. Stoyanova, M. Gorova and E. Zhecheva, *J. Phys. Chem. Solids*, submitted.
39 C. Masquelier, M. Tabuchi, K. Ado, R. Kanno, Y. Kobayashi, Y. Maki, O. Nakamura and J. B. Goodenough, *J. Solid State Chem.*, 1996, **123**, 255.
40 K. D. Singh, S. C. Jain, T. D. Sakore and A. B. Biswas, *Acta Crystallogr.*, *Sect. B*, 1975, **31**, 990.
41 T. Lis, *Acta Crystallogr.*, *Sect. B*, 1982, **38**, 937.
42 R. Swanson, W. H. Ilsey and A. G. Stanislowski, *J. Inorg. Biochem.*, 1983, **18**, 187.
43 R. C. Bott, D. S. Sagatys, D. E. Lynch, G. Smith, C. H. L. Kennard and T. C. W. Mak, *Aust. J. Chem.*, 1991, **44**, 1495.
44 J. P. Glusker and H. L. Carrell, *J. Mol. Struct.*, 1973, **15**, 151.
45 A. Karipides and A. T. Reed, *Inorg. Chem.*, 1976, **15**, 44.
46 Y. Xia and M. Yoshio, *J. Electrochem. Soc.*, 1997, **144**, 4186.
47 S. Angelov, E. Zhecheva and D. Mehandjiev, *Commun. Dep. Chem. Bulg. Acad. Sci.*, 1980, **13**, 369.
48 C. Pirovano and S. Trasatti, *J. Electroanal. Chem: Interfacial Electrochem.*, 1984, **180**, 171.

Paper 9/00076C